Optics Letters

Multi-band on-chip photonic spin Hall effect and selective excitation of whispering gallery modes with metasurface-integrated microcavity

Yuebian Zhang,[1] Zhancheng Li,[1] Wenwei Liu,[1] Zhi Li,[1] Hua Cheng,[1,2,4] Jianguo Tian,[1,2,5] and Shuqi Chen[1,2,3,*]

[1]The Key Laboratory of Weak Light Nonlinear Photonics, Ministry of Education, School of Physics and TEDA Institute of Applied Physics, Nankai University, Tianjin 300071, China
[2]The Collaborative Innovation Center of Extreme Optics, Shanxi University, Taiyuan, Shanxi 030006, China
[3]The Collaborative Innovation Center of Light Manipulations and Applications, Shandong Normal University, Jinan 250358, China
[4]e-mail: hcheng@nankai.edu.cn
[5]e-mail: jjtian@nankai.edu.cn
*Corresponding author: schen@nankai.edu.cn

Received 27 April 2021; revised 17 June 2021; accepted 20 June 2021; posted 23 June 2021 (Doc. ID 429940); published 20 July 2021

We propose an approach to realize a multi-band on-chip photonic spin Hall effect and selective excitation of whispering gallery modes (WGMs) by integrating metasurfaces with microcavities. Free-space circularly polarized light with opposite spin angular momentum can effectively excite WGMs with opposite propagation directions at fixed wavelengths. Moreover, the different WGMs with different propagation directions and polarizations can be selectively excited by manipulating the number of antennas. We demonstrate that the optical properties (i.e., coupling efficiency, peak positions, and peak widths) of the proposed metasurface-integrated microcavities can be easily tailored by adjusting different geometric parameters. This study enables the realization of chiral microcavities with exciting novel functionalities, which may provide a further step in the development of photonic integrated circuits, optical sensing, and chiral optics.

https://doi.org/10.1364/OL.429940

Optical whispering gallery mode (WGM) microcavities can confine light in a small volume for a long time, so they can greatly enhance the interaction between light and matter, which have been widely used in sensing [1], lasers [2], nonlinear optics [3], and other fields. Due to the symmetry of optical WGM microcavities, it is difficult to realize direct coupling between free-space light and microcavity mode. Instead, optical fibers and waveguides are usually used to couple light into or from the microcavity [4]. However, these coupling methods always require precise alignment of the optical fibers with nano-positioning systems or additional optical components to couple light into the waveguide, which limits the application scenarios of microcavities. In addition, coupling of vertical free-space light to a microcavity is desirable in many applications, such as solar powered on-chip photonics devices and wireless optical communication devices. One way to couple free-space light into microcavities is to use deformed microcavities [5]. However, this method also requires precise alignment processes. Another method is to deposit nano-scatterers or nanoparticles onto the microcavities [6,7]. However, this method has limited ability to manipulate the microcavity light field.

Metasurfaces are artificial surfaces composed of subwavelength microstructures arranged in regular patterns, which can manipulate the amplitude, polarization, and phase of wave fields arbitrarily [8–11]. More importantly, the nano-antennas of metasurfaces can be used as bridges between free-space light and guided electromagnetic waves, so as to expand the application scope of traditional on-chip photonics devices [12–15]. Recently, Lawrence *et al.* experimentally demonstrated that high-quality-factor phase gradient metasurfaces can be realized by exciting and manipulating guided modes with free-space light [16]. However, the potentialities of metasurfaces in manipulating the microcavity light field have not been fully exploited. How to use metasurfaces to realize the conversion between free-space light and WGMs remains to be studied [17,18]. The photonic spin Hall effect (PSHE) is an important effect referring to the lateral separation of left-handed circularly polarized (LCP) and right-handed circularly polarized (RCP) photons [19], which can be used in multifunctional photonics devices, optical information processing, and multiplexing. The PSHE originates from the spin–orbit interaction of light [20,21], which can be realized and enhanced with metasurfaces [22]. More interestingly, the spin angular momentum (SAM) of photons can be orthogonal to the propagation direction of light in evanescent near fields and guided waves, which is called transverse SAM [23,24]. Although many PSHEs have been realized in reflective and transmitted schemes [25–27], realizing the multi-band on-chip PSHE remains a major challenge for researchers. Recently, several works have demonstrated that dual-band on-chip PSHE can be realized by integrating metasurfaces with waveguides [13,14]. However, the working bandwidths of these works are wide, which limits the practical application of these devices in wavelength de-multiplexing.

The resonant wavelengths of microcavities are discrete, and the quality factors of WGMs are higher compared with those of the waveguide. Therefore, by integrating metasurfaces with microcavities, we can realize not only direct coupling between free-space light and microcavities, but also multi-band on-chip PSHE with a narrow bandwidth. In addition, by introducing subwavelength microstructures into on-chip microcavities, more degrees of freedom in the manipulation of microcavity light fields can be introduced, which can provide new opportunities for the realization of novel on-chip photonics devices.

In this paper, we propose and demonstrate a novel approach to realize four-band on-chip PSHE by integrating metasurfaces with microcavities. WGMs with opposite propagation directions can be excited by free-space circularly polarized (CP) light with opposite SAM at fixed wavelengths. Moreover, both transverse electric (TE) and transverse magnetic (TM) WGMs can be selectively excited and separated into opposite directions by the incident CP light at different wavelengths. We demonstrate that the optical properties of the proposed metasurface-integrated microcavities (MIMs) can be easily tailored by adjusting different geometric parameters. This study could provide a further step in the development of photonic integrated devices [28], optical sensing [29], chiral optics [30–32], and nonlinear optics [33,34], and may result in novel functionalities for nano-photonic devices.

The structure of the proposed MIM is shown in Fig. 1. It comprises a SiO_2 substrate, Si_3N_4 waveguide, Si_3N_4 microcavity, $N = 120$ Al nanorods, and a coating layer. The waveguide has width $w = 1600$ nm and thickness $t = 700$ nm. The radius of the microdisk is $R = 12$ μm, and its thickness is $t = 700$ nm. The gap between the microdisk and waveguide is $g = 200$ nm. The length, width, and height of each Al nanorod are $a = 360$ nm, $b = 110$ nm, and $h = 80$ nm, respectively. The distance between these nanorods and the center of the microdisk is $r = 10.5$ μm, and the positions of these nanorods can be described by using the local coordinates (r, φ, z). The rotation angle of a nanorod at position (r, φ) is $\theta(\varphi) = \varphi \pm \frac{\pi}{2} \cdot \frac{\varphi}{\Delta\varphi} = \varphi \pm N\varphi/4$, where $\Delta\varphi = 2\pi/N$ is the azimuthal angle difference between two adjacent nanorods. The numerical simulations were conducted using a finite difference time-domain approach based on the Lumerical Solutions commercial software package. Two total-field-scattered-field sources with a cross-sectional area of 24.1 μm × 24.1 μm were used to simulate the incident free-space CP plane wave. Two power monitors were located at $x = \pm 15$ μm to record the power through the waveguide. The coupling efficiencies of the MIMs are defined as the ratio of the power recorded by the power

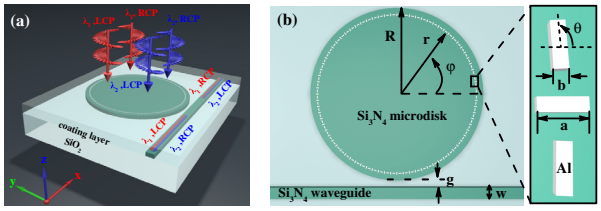

Fig. 1. (a) Schematic of the MIM. At a fixed wavelength, CP light with opposite SAM can excite WGMs with opposite propagation directions. In addition, WGMs with different propagation directions can be selectively excited at different wavelengths. (b) Plan view and geometric parameters of the MIM.

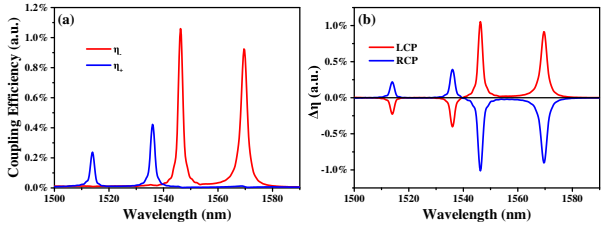

Fig. 2. (a) Coupling efficiency spectra toward different sides of the waveguide for RCP incidence. η_+/η_- corresponds to light propagating along the $+x/-x$ direction. (b) Coupling efficiency difference $\Delta\eta$ for different CP incident light.

monitors to the incident power: $\eta = P_{\text{monitor}}/P_{\text{in}}$. It should be noted that, because the antennas cover only a small area (about 6%) of the microcavity, only a small fraction of the incident light can shine on the nano-antennas. Therefore, the absolute value of the coupling efficiency cannot reflect the actual ability of the antenna to couple free-space light. The coupling efficiency difference between two opposite directions is more valuable, which is defined as $\Delta\eta = \eta_+ - \eta_-$. The optical constant of Al was taken from Ref. [35]. The refractive indices of Si_3N_4 and the SiO_2 substrate are 1.927 and 1.44, respectively. A coating layer with a refractive index of 1.44 was used to prevent the Al nanorods from oxidation. In our simulation, the thickness of the SiO_2 substrate is assumed to be infinite, and the thickness of the coating layer is 1.5 μm.

Figure 2(a) shows the coupling efficiency spectra toward different sides of the waveguide for RCP incident light. It can be seen that there are four resonance peaks in the range of 1500–1590 nm, which are at about 1514.0 nm, 1536.0 nm, 1546.3 nm, and 1569.5 nm. The incident lights at 1514.0 nm and 1536.0 nm are mainly coupled to the $+x$ direction of the waveguide, corresponding to counterclockwise (CCW) WGMs. The incident lights at 1546.3 nm and 1569.5 nm are mainly coupled to the $-x$ direction of the waveguide, which corresponds to clockwise (CW) WGMs. Therefore, the MIM can be used to distinguish and separate incident lights with different wavelengths. We further calculated the coupling efficiency difference $\Delta\eta$ for different CP incident lights, and the result is shown in Fig. 2(b). When the incident light is changed from RCP to LCP, the propagation directions of the WGMs and waveguide modes at the four resonance peaks will change into opposite directions, indicating that the directional coupling microcavity has "chirality." The coupling efficiencies can remain the same when the spin state of incident light is flipped. The proposed MIM can realize multi-band PSHE, and the propagation direction of the photon can be opposite at different wavelengths, which is quite different from the PSHE realized only by geometric phase metasurfaces [25–27].

To study the excited microcavity modes and waveguide modes, we plot the electric field amplitude distributions $|\vec{E}|$ in the x-y plane bisecting the waveguide and microcavity for RCP and LCP incidence at 1536.0 nm and 1546.3 nm, respectively, in Fig. 3. It can be seen that the RCP and LCP incident lights are mainly coupled to the $+x$ and $-x$ directions of the waveguide at a wavelength of 1536.0 nm, respectively, while the RCP and LCP incident lights are mainly coupled to the $-x$ and $+x$ directions of the waveguide at 1546.3 nm, which is consistent with the coupling efficiency spectra in Fig. 2. These results demonstrate that the MIM can simultaneously achieve spin-selective

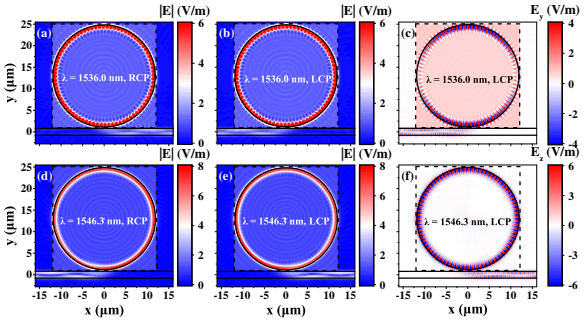

Fig. 3. Electric field amplitude distributions $|\vec{E}|$ in the x-y plane bisecting the waveguide and microcavity for (a) RCP incidence and (b) LCP incidence at 1536.0 nm. (c) E_y distribution in the x-y plane for LCP incidence at 1536.0 nm. Electric field amplitude distributions $|\vec{E}|$ in the x-y plane for (d) RCP incidence and (e) LCP incidence at 1546.3 nm. (f) E_y distribution in the x-y plane for LCP incidence at 1546.3 nm. Black solid lines and black dashed lines show the boundaries of the MIM and incident light region, respectively.

and wavelength-selective directional coupling. Figures 3(c) and 3(f) show the electric field components of the excited waveguide and microcavity modes. The electric fields are dominated by E_x and E_y at 1536.0 nm, indicating that the excited microcavity mode is TE. The electric field of the excited microcavity mode is dominated by E_z at 1546.3 nm, indicating that the excited microcavity mode is TM. In Figs. 3(c) and 3(f), we can also see that the excited waveguide modes at 1536.0 nm and 1546.3 nm are TE_{10} and TM_{10}, respectively. In fact, the output waveguide modes can be easily manipulated by tailoring the width of the waveguide. For example, if the width of the waveguide is reduced to 800 nm, the output waveguide modes at 1536.0 nm and 1546.3 nm would be TE_{00} and TM_{00}, respectively.

To further study the origin of spin-selective and wavelength-selective directional coupling, we simulated the transmission spectra of the microcavity when light is injected from one end of the waveguide. As shown in Fig. 4(a), there are five transmission dips in the range of 1510–1590 nm under TE_{10} or TM_{10} waveguide mode excitation, which correspond to five different WGMs. We use Em and Mm to name the WGMs excited by TE and TM waveguide modes, where m is the azimuthal mode number of each WGM. As shown in Fig. 4(a), WGMs excited by TE_{10} waveguide mode are $E_{78} - E_{82}$, and WGMs excited by TM_{10} waveguide mode are $M_{77} - M_{81}$. In Fig. 4(a), we can also see that WGMs at about 1514.0 nm, 1536.0 nm, 1546.3 nm, and 1569.5 nm are M_{81}, E_{81}, M_{79}, and E_{79}, respectively. That is to say, if free-space light is vertically incident onto the MIM, only specified WGMs can be selectively excited. In fact, this phenomenon can be explained by the phase-matching between the scattering field of the metasurface and the WGMs of the microcavity. When CP light is vertically incident from the air onto the MIM, the Pancharatnam-Berry (P-B) phase distribution provided by the metasurface can be written as [8–10,36]

$$\Phi_N(\varphi) = \pm\frac{N}{2}\varphi + 2\sigma\varphi, \tag{1}$$

where N is the number of Al nanorods, and $\sigma = \pm 1$ corresponds to RCP and LCP incident lights, respectively. The term "$\pm N\varphi/2$" indicates that the Al nanorod array can provide two transverse wave vectors. When "+" is taken, the transverse wave vector is along the CCW direction. When "−" is taken, the transverse wave vector is along the CW direction. The optical field of WGM has transverse SAM, which is locked with the momentum (propagation direction) of the WGM [37]. Here we define the local transverse spin state of the WGM field as

$$\sigma' = \frac{|E_r + iE_\varphi|^2 - |E_r - iE_\varphi|^2}{|E_r - iE_\varphi|^2 + |E_r + iE_\varphi|^2}, \tag{2}$$

where E_r and E_φ represent the local transverse and longitudinal polarized components of the optical field in the microcavity, and $\sigma' = \pm 1$ corresponds to the optical field with local transverse spin states rotating along CW or CCW direction, respectively. When the excited WGM is CCW mode, the phase distribution of the mode in the microcavity can be written as $\Phi_m(\varphi) = m\varphi + \sigma'\varphi$, where m is the azimuthal mode number of the WGM. The term "$m\varphi$" represents the propagation phase of the CCW mode, and the second term represents the geometric phase arising from the rotation of the local transverse-spin state while WGMs travel along the microcavity. Therefore, when the P-B phase distribution provided by the metasurface is matched with the phase distribution of the CCW mode, i.e.,

$$\frac{N}{2} + 2\sigma = m + \sigma', \tag{3}$$

the incident CP light will excite the CCW WGMs. Similarly, the phase distribution of the CW mode in the microcavity can be written as $\Phi_m(\varphi) = -m\varphi + \sigma'\varphi$. Therefore, when the phase-matching condition

$$-\frac{N}{2} + 2\sigma = -m + \sigma' \tag{4}$$

is met, the incident CP light will excite the CW WGMs. When the incident light is RCP light, both the local electric field vector of the converted LCP transmission light and the local transverse-spin state of the excited WGM will rotate CW (view from the top of the microcavity). In this situation, $\sigma = 1$ and $\sigma' = 1$. According to Eqs. (3) and (4), the excited CCW modes and CW modes can be obtained as $m = N/2 + 1$ and $m = N/2 - 1$, respectively. Similarly, for LCP incident light, $\sigma = -1$ and $\sigma' = -1$; as a result, the excited CCW modes and CW modes can be obtained as $m = N/2 - 1$ and $m = N/2 + 1$, respectively. To verify the above theory, we simulated the coupling efficiency difference $\Delta\eta$ of WGMs excited by LCP light when the number of Al nanorods was 158, 160, and 162. As shown in Fig. 4(b), when $N = 158$, the excited CCW WGMs are M_{78} and E_{78} that output along the $+x$ direction of the waveguide, and the excited CW WGMs are M_{80} and E_{80} that output along the $-x$ direction of the waveguide. When $N = 160$ and $N = 162$, the excited WGMs also agree well with theoretical predictions. These results show that we can selectively excite specific WGMs by manipulating the number of nanorods, and different WGMs with different modfe numbers m can be separated through different directions of the waveguide. In addition, the WGMs' outputs along the same direction have different polarizations and wavelengths, which also facilitates the separation of these modes. The selective excitation and directional coupling of different WGMs may give birth to new types of on-chip integrated multifunctional photonic devices.

To further study the effect of different geometric parameters on the performance of the MIM, we simulated the coupling efficiency difference $\Delta\eta$ for different antenna positions r and

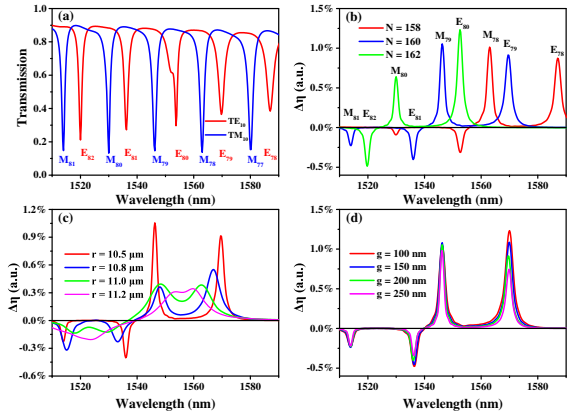

Fig. 4. (a) Transmission spectra of the MIM for TE_{10} and TM_{10} waveguide modes excitation. Coupling efficiency difference $\Delta\eta$ for (b) different numbers of antennas N, (c) different antenna positions r, and (d) different gaps g.

different gaps g under LCP incidence. Figure 4(c) shows that the peak width of different resonance peaks becomes wider when the Al nanorod arrays move closer to the edge of the microcavity. This is mainly due to the increasing interaction between the nanorods and the WGM fields as the nanorods move toward the edge of the microcavity, which leads to increasing disturbance of the nanorods to the WGMs and increasing radiation loss of the modes. The gap g between the microcavity and waveguide mainly affects the coupling efficiency between WGMs and waveguide modes. As shown in Fig. 4(d), when the gap g increases from 100 nm to 250 nm, the coupling efficiency difference $\Delta\eta$ of the structure decreases gradually, and the WGMs of TE polarization are more sensitive to the change in gap g. These results further show that the coupling efficiency, peak positions, and peak widths of the MIM can be easily tailored by adjusting different geometric parameters.

In conclusion, based on the MIM, incident free-space photons with different spin states can be routed to opposite directions of the waveguide at fixed wavelengths, and the propagation direction of the photons with the same spin state can be opposite at different wavelengths. In addition, by manipulating the number of antennas, different WGMs can be selectively excited and routed to different directions. The excited WGMs are determined by the phase-matching condition between the scattering field of the metasurface and the WGMs of the microcavity. Moreover, incident CP light can excite both TE and TM WGMs and direct them into opposite directions. We demonstrate that the optical properties of the proposed MIMs can be easily tailored by adjusting different geometric parameters. The proposed MIM system can provide a new platform to connect free-space light and a microcavity light field, or to further study the interaction between SAM and orbital angular momentum, which may give birth to new types of on-chip integrated photonic devices.

Funding. National Key Research and Development Program of China (2016YFA0301102, 2017YFA0303800); National Science Fund for Distinguished Young Scholars (11925403); National Natural Science Foundation of China (11774186, 11974193, 91856101); China Postdoctoral Science Foundation (2020M680851); Natural Science Foundation of Tianjin City for Distinguished Young Scientists (18JCJQJC45700).

Disclosures. The authors declare no conflicts of interest.

Data Availability. Data underlying the results presented in this paper are not publicly available at this time but may be obtained from the authors upon reasonable request.

REFERENCES

1. M. R. Foreman, J. D. Swaim, and F. Vollmer, Adv. Opt. Photon. **7**, 168 (2015).
2. X.-F. Jiang, C.-L. Zou, L. Wang, Q. Gong, and Y.-F. Xiao, Photon. Rev. **10**, 40 (2016).
3. T. J. Kippenberg, A. L. Gaeta, M. Lipson, and M. L. Gorodetsky, Science **361**, eaan8083 (2018).
4. L. Cai, J. Pan, and S. Hu, Opt. Laser Eng. **127**, 105968 (2020).
5. L. Shao, X. F. Jiang, X. C. Yu, B. B. Li, W. R. Clements, F. Vollmer, W. Wang, Y. F. Xiao, and Q. Gong, Adv. Mater. **25**, 5616 (2013).
6. J. Zhu, S. K. Ozdemir, H. Yilmaz, B. Peng, M. Dong, M. Tomes, T. Carmon, and L. Yang, Sci. Rep. **4**, 6396 (2014).
7. F. Gu, L. Zhang, Y. Zhu, and H. Zeng, Laser Photon. Rev. **9**, 682 (2015).
8. S. Chen, Z. Li, W. Liu, H. Cheng, and J. Tian, Adv. Mater. **31**, 1802458 (2019).
9. S. Chen, W. Liu, Z. Li, H. Cheng, and J. Tian, Adv. Mater. **32**, 1805912 (2020).
10. Z. Li, W. Liu, H. Cheng, and S. Chen, Sci. China Phys. Mech. **63**, 284202 (2020).
11. A. C. Overvig, S. Shrestha, and N. Yu, Nanophotonics **7**, 1157 (2018).
12. R. Guo, M. Decker, F. Setzpfandt, X. Gai, D. Y. Choi, R. Kiselev, A. Chipouline, I. Staude, T. Pertsch, D. N. Neshev, and Y. S. Kivshar, Sci. Adv. **3**, e1700007 (2017).
13. Y. Zhang, Z. Li, W. Liu, Z. Li, H. Cheng, S. Chen, and J. Tian, Adv. Opt. Mater. **7**, 1801273 (2019).
14. Y. Meng, Z. Liu, Z. Xie, R. Wang, T. Qi, F. Hu, H. Kim, Q. Xiao, X. Fu, Q. Wu, S.-H. Bae, M. Gong, and X. Yuan, Photon. Res. **8**, 564 (2020).
15. X. Guo, Y. Ding, X. Chen, Y. Duan, and X. Ni, Sci. Adv. **6**, eabb4142 (2020).
16. M. Lawrence, D. R. Barton, J. Dixon, J.-H. Song, J. van de Groep, M. L. Brongersma, and J. A. Dionne, Nat. Nanotechnol. **15**, 956 (2020).
17. H. M. Doeleman, E. Verhagen, and A. F. Koenderink, ACS Photon. **3**, 1943 (2016).
18. K. G. Cognee, H. M. Doeleman, P. Lalanne, and A. F. Koenderink, Light: Sci. Appl. **8**, 1 (2019).
19. Y. Liu, Y. Ke, H. Luo, and S. Wen, Nanophotonics **6**, 51 (2017).
20. K. Y. Bliokh, F. J. Rodríguez-Fortuño, F. Nori, and A. V. Zayats, Nat. Photonics **9**, 796 (2015).
21. K. Y. Bliokh, D. Smirnova, and F. Nori, Science **348**, 1448 (2015).
22. X. Ling, X. Zhou, X. Yi, W. Shu, Y. Liu, S. Chen, H. Luo, S. Wen, and D. Fan, Light: Sci. Appl. **4**, e290 (2015).
23. K. Y. Bliokh and F. Nori, Phys. Rev. A **85**, 061801 (2012).
24. K. Y. Bliokh and F. Nori, Phys. Rep. **592**, 1 (2015).
25. X. Yin, Z. Ye, J. Rho, Y. Wang, and X. Zhang, Science **339**, 1405 (2013).
26. Z. Li, W. Liu, H. Cheng, S. Chen, and J. Tian, Adv. Opt. Mater. **5**, 1700413 (2017).
27. W. Luo, S. Xiao, Q. He, S. Sun, and L. Zhou, Adv. Opt. Mater. **3**, 1102 (2015).
28. B. Xu, H. Li, S. Gao, X. Hua, C. Yang, C. Chen, F. Yan, S. Zhu, and T. Li, Adv. Photon. **2**, 066004 (2020).
29. Y. Zhao, A. N. Askarpour, L. Sun, J. Shi, X. Li, and A. Alu, Nat. Commun. **8**, 14180 (2017).
30. A. Y. Zhu, W. T. Chen, A. Zaidi, Y.-W. Huang, M. Khorasaninejad, V. Sanjeev, C.-W. Qiu, and F. Capasso, Light: Sci. Appl. **7**, 17158 (2018).
31. M. V. Gorkunov, A. A. Antonov, and Y. S. Kivshar, Phys. Rev. Lett. **125**, 093903 (2020).
32. J. Dixon, M. Lawrence, D. R. Barton, and J. Dionne, Phys. Rev. Lett. **126**, 123201 (2021).
33. B. Sain, C. Meier, and T. Zentgraf, Adv. Photonics **1**, 1 (2019).
34. S. Rubin and Y. Fainman, Adv. Photonics **1**, 1 (2019).
35. E. D. Palik, *Handbook of Optical Constants of Solids* (Academic, 1985), Vol. **I**.
36. L. Huang, X. Chen, H. Mühlenbernd, G. Li, B. Bai, Q. Tan, G. Jin, T. Zentgraf, and S. Zhang, Nano Lett. **12**, 5750 (2012).
37. Z. Shao, J. Zhu, Y. Chen, Y. Zhang, and S. Yu, Nat. Commun. **9**, 926 (2018).